Multipoint Aerodynamic Shape Optimization Investigations of the Common Research Model Wing

Gaetan K. W. Kenway[*] and Joaquim R. R. A. Martins[†]

Department of Aerospace Engineering, University of Michigan, Ann Arbor, MI

Aerodynamic shape optimization of wings in transonic flow is an inherently challenging problem. In addition to the high computational cost of solving the Reynolds-averaged Navier–Stokes (RANS) equations, there is a complex interdependence between the cross-sectional shape, wave drag and viscous effects. Furthermore, it is necessary to perform multipoint optimizations to ensure good performance for a range of flight conditions. The choice of which flight conditions should be considered in the multipoint optimization, and how many points should be considered is still not understood. We address this issue by solving a series of six benchmark optimizations developed by the Aerodynamic Shape Optimization Discussion Group. These optimization cases include a single point optimization, four 3-point optimizations, and a 9-point optimization. The optimization consists in minimizing the weighted drag coefficient subject to lift, moment, thickness, and volume constraints. The optimizations are performed with respect to 768 shape design variables, and an angle of attack for each flight condition. The single point optimization was able to achieve a 7.5% drag reduction relative to the initial design, but it exhibits poor off-design performance. All optimized designs were compared using a contour plot of ML/c_D to evaluate the wing performance over the complete transonic flight operating envelope. Each of the four 3-point optimizations successfully mitigated the poor off-design performance of the single point design. However, the 3-point optimization with widely spaced Mach numbers yielded a much more complex ML/c_D contour with two distinct local maxima. Finally, the 9-point optimization yielded the most robust off-design performance.

I.   Introduction

Recent advances in high performance computing have enabled the deployment of full-scale physics-based numerical simulations and optimization in academia and industry. Computational fluid dynamics (CFD) tools and numerical optimization techniques have been widely adopted to shorten design cycle times and to explore design spaces more effectively. High-fidelity methods enable engineers to perform detailed designs earlier in the design process, allowing them to better understand the design trade-offs and to make more informed design decisions. In addition, advances in sensitivity analysis via the adjoint method [1, 2, 3, 4, 5] have dramatically reduced the computational effort required for aerodynamic shape optimization.

In spite of over two decades of research, we still do not fully understand which problem formulations should be used to obtain practical aerodynamic designs, and what are the best strategies for solving aerodynamic shape optimization problems. Also, performing aerodynamic shape optimization based on the Reynolds-averaged Navier–Stokes (RANS) equations on a large grid size remains a challenging task. To make a collective effort towards a better understanding of aerodynamic shape optimization, the Aerodynamic Design Optimization Discussion Group (ADODG) developed a series of benchmark problems that range from two-dimensional airfoil optimization based on the Euler equations to three-dimensional wing shape optimization based on the RANS-equations[a].

We have previously presented the results for the single-point RANS-based aerodynamic shape optimization of the Common Research Model (CRM), and made our optimal geometries and meshes publicly available [6][b]. These results were obtained using the aerodynamic shape optimization framework that we had previously developed [7, 8], which

---

*Post-doctoral Research Fellow, Department of Aerospace Engineering, University of Michigan, AIAA Member

†Associate Professor, Department of Aerospace Engineering, University of Michigan, AIAA Associate Fellow

[a]https://info.aiaa.org/tac/ASG/APATC/AeroDesignOpt-DG/default.aspx, last accessed Dec 1, 2014

[b]http://mdolab.engin.umich.edu/content/aerodynamic-design-optimization-workshop, last accessed Dec 1, 2014

uses gradient-based optimization together with a discrete adjoint to compute the gradients efficiently. The aerodynamic shape optimization framework has also been coupled to a structural finite-element solver to enable aerostructural design optimization [9, 10, 11].

When solving the single-point aerodynamic shape optimization of the CRM wing, we also studied the existence of multiple local minima, and we found that while there are multiple local minima, the differences in optimal drag coefficients and in the design shape are negligible: the differences in optimal drag coefficients were within 0.1 counts (0.05% of the minimum drag), while the L_2 norm of the differences in the shape were less than 1% of the mean aerodynamic chord [6]. In addition to the solution of the single-point optimization problem developed by the ADODG, we also added a 5-point multipoint optimization, which resulted in a much more robust aerodynamic design, as demonstrated by evaluating the performance of all optimal designs in Mach–C_L space. Finally, we also presented a multilevel optimization technique, studied the effect of the number of design variables, and solved a case with larger thickness constraints [6]. Other researchers presented their solutions to the single-point CRM wing optimization in the same ADODG special session at the AIAA SciTech 2014 conference [12, 13, 14].

To further explore multipoint aerodynamic shape optimization, the ADODG developed a series of six different multipoint cases for the RANS-based optimization of the CRM wing. We solve all six multipoint cases in the present paper, and compare the performance of the resulting designs by making contour plots of ML/cD.

The paper is organized as follows. The numerical tools used in this work are described in Section II. The problem formulation, mesh, and initial geometry are described in Section III. The results of the six multipoint ADODG optimizations are given in Section IV, followed by the conclusions.

II.   Methodology

We briefly describe the computational framework used for aerodynamic shape optimization. The tools used herein are a subset of the multidisciplinary design optimization (MDO) of aircraft configurations with high fidelity (MACH) [9, 15] framework, which has been successfully employed by the authors to solve aerodynamic design optimization [16, 17, 18, 6] and aerostructural design optimization problems [9, 10, 11, 19].

A.   Geometric Parametrization

Many different geometric parameterization techniques have been successfully used in the past for aerodynamic shape optimization. These include mesh coordinates (with smoothing) [12], B-spline surfaces [20], Hicks–Henne bump functions [21], camber-line-thickness parameterization [14], and free-form deformation (FFD) [22]. The only requirement specified by the ADODG for the parameterization is that the planform must remain fixed and the changes in shape may only be made in the vertical (z) direction. All of the aforementioned techniques can satisfy these requirements if implemented correctly. In this work we use an FFD volume approach that we have implemented [22] and have used extensively [16, 17, 18, 6, 9, 10, 11, 19].

The FFD approach can be visualized as embedding the spatial coordinates defining a geometry inside a flexible volume. The parametric locations (u, v, w) corresponding to the initial geometry are found using a Newton search algorithm. Once the initial geometry is embedded, perturbations made to the FFD volume propagate within the embedded geometry by evaluating the nodes at their parametric locations. We use tri-variate B-spline volumes for the FFD implementation, and use displacement of the control point locations as design variables. The sensitivity of the geometric location of the geometry with respect to the control points is computed efficiently using analytic derivatives of the B-spline shape functions [23].

Two different FFD volumes are used in this work. The first is a coarse FFD with 192 control points arranged in a $12 \times 8 \times 2$ pattern, corresponding to the chord-wise, spanwise and vertical directions, respectively, as show on the left of Figure 1. This FFD is used for the initial coarse grid (named the L2 grid) optimization described in Section A. The second FFD is based on a finer pattern ($24 \times 16 \times 2$)—shown on the right of Figure 1—and this FFD is used for all fine (L1) grid optimizations. A linear least squares minimization is used to interpolate the optimized result from the coarse FFD to the fine FFD before the optimization begins. Both FFD volumes are shown in Figure 1.
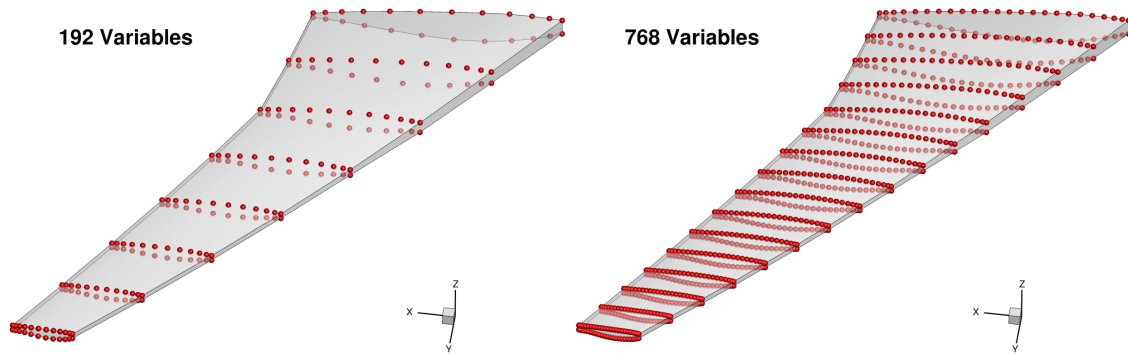
Figure 1. The fine FFD (right) has 4 times the number of control points as the coarse FFD (left).

B. Mesh Perturbation

The FFD approach we just described only applies deformations to the surface mesh, that is, the part of the volume mesh that lies on the wing surface. A separate operation is performed to propagate these perturbations to the remainder of the volume mesh. Due to the simple O-grid topology used for our grids, and because the surface changes to the fixed planform are relatively small, a simple algebraic method based on transfinite interpolation was found to be sufficient. This method is a simplification of the more complex hybrid algebraic-linear elasticity method described by Kenway *et al.* [24], which can handle larger shape changes.

C. CFD Solver

The flow solver used in this work is SUmb [25], a finite-volume, cell-centered multiblock solver for the compressible RANS equations. The Jameson–Schmidt–Turkel (JST) artificial dissipation scheme [26] is employed with coefficients of $1/64$ and $1/4$ for the 4th order and 2nd order terms, respectively. The Spalart–Allmaras (SA) turbulence model [27] is used and is coupled to the mean flow in a segregated fashion. A diagonally dominant alternating direction implicit (DDADI) method is used for both the mean flow and turbulence equations. A discrete adjoint method implemented using algorithmic differentiation is used for the efficient computation of gradients of the functions of interest. More details on this adjoint implementation are provided by Lyu *et al.* [8].

D. Optimization Algorithm

The high computational cost of RANS CFD solutions dictates that the optimization should require a reasonably low number of function calls. Some gradient-free methods, such as genetic algorithms, have a higher probability of getting close to the global minimum for cases with multiple local minima and low number of design variable. However, a previously mentioned, our experience with the optimization of the CRM wing has failed to show significant local minima, and thus the use of gradient based optimization is justified [6, 28].

The optimization algorithm we use is SNOPT (sparse nonlinear optimizer) [29], through the Python interface py-Opt [30] for all results presented here. SNOPT is a gradient-based optimizer that implements a sequential quadratic programming method; it is capable of solving large-scale nonlinear optimization problems with thousands of constraints and design variables. SNOPT uses a augmented Lagrangian merit function, and the Hessian of the Lagrangian is approximated using a quasi-Newton method.
-

III.   Problem Description

The ADODG currently defines four optimization problems of increasing computational complexity[c]:

---

[c]https://info.aiaa.org/tac/ASG/APATC/AeroDesignOpt-DG/default.aspx, last accessed Dec 1, 2014

3

Case 1: 2D Euler-based drag minimization of NACA 0012 profile in transonic flow

Case 2: 2D RANS-based drag minimization of RAE2822 profile in transonic flow

Case 3: 3D inviscid drag minimization of $AR = 6$ wing NACA 0012 cross section in subsonic flow

Case 4: 3D RANS-based drag minimization of the CRM wing in transonic flow (single point and multipoint)

The first few studies of Case 1 showed that this case is surprisingly challenging [12, 13, 14]. Minute changes in the airfoil profile can yield large changes in the shock structure and correspondingly large changes in the optimized drag. While this case is interesting from an academic perspective, due to the idealization of two dimensional Euler flow, this case has little practical engineering value. Similar arguments can be made for Cases 2 and 3.

We have chosen to focus on Case 4, which is the most physically realistic, and the most demanding in terms of computational cost. Despite the increased computational cost of analyzing three-dimensional turbulent RANS flow, we have found that this case tends to be easier from an optimization perspective, as the optimization algorithm is less likely to exploit physical shortcomings of the underlying numerical model.

A.   Initial Geometry

The initial geometry is a wing with a blunt trailing edge extracted from the CRM geometry. The geometry and specifications are given by the ADODG [20]. The fuselage and tail are deleted from the original CRM, and the root of the remaining wing is moved to the symmetry plane. The initial geometry is shown in Figure 2. All coordinates are scaled by the mean aerodynamic chord (275.8 in). The reference wing area is 3.407014 and the point about which the pitching moment is taken is $(x, y, z) = (1.2077, 0.0, 0.007669)$.
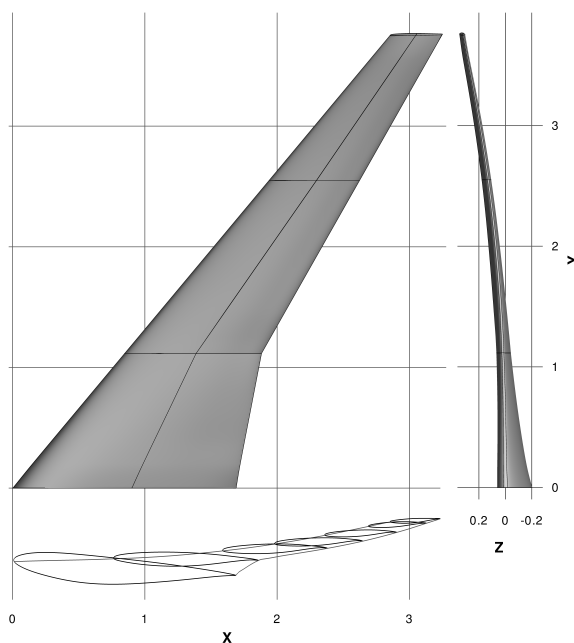

Figure 2. Initial geometry scaled by its mean aerodynamic chord.

B.   Computational Grids

A sequence of CFD meshes were generated using an in-house hyperbolic mesh generator. The computational technique used in the meshing scheme follows the work of Chan and Steger [31]. The three-dimensional multi-block mesh

4

is generated by marching a multi-block patching on the wing surface a sufficient distance away from the wing—automatically generating an O-type topology. For all cases, the far field boundary is located at a distance of 25 times the wing semi-span. The off-wall spacing is set to ensure a maximum y^+ value of less than one for the L1 grid at the nominal operating condition of $Re = 5$ million and a Mach number of 0.85.

A family of three uniformly refined meshes were generated with sizes ranging from 450 k cells to over 28 M cells (see Table 1 for the exact numbers). The surface mesh and symmetry plane for each of the meshes is shown in Figure 3. Only the two smaller grids (L2 and L1) are considered for optimization, and the largest one (L0) is used for the grid convergence study.
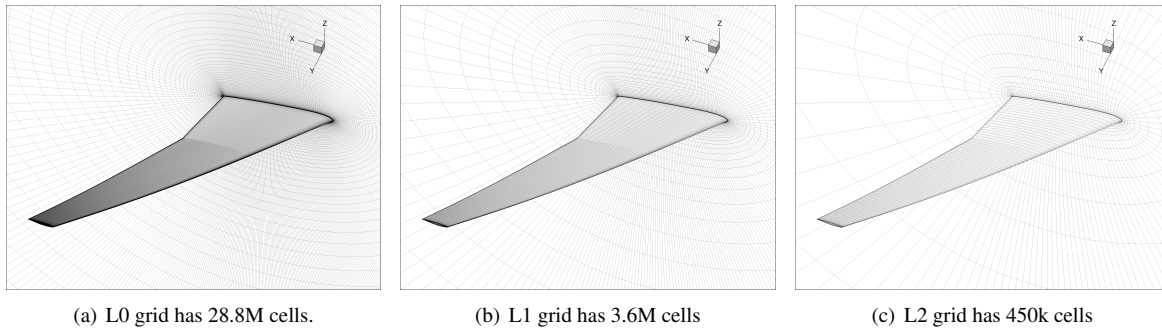

(a) L0 grid has 28.8M cells. (b) L1 grid has 3.6M cells (c) L2 grid has 450k cells

Figure 3. O-grids of varying sizes were generated using an hyperbolic mesh generator.

A grid convergence study was performed using the initial geometry and the optimized grid from case 4.1 (see Table 2). For the optimized configuration, the design variables from the L1 geometry are applied to the L0 and L2 grids. For this reason, the L2 drag for the optimized configuration is slightly higher than the result from the actual L2 optimization (see Figure 5). The zero-grid spacing result is computed by extrapolating the two finest grid results, which are assumed to lie within the asymptotic convergence region. The difference between the extrapolated zero-grid spacing value and the L1 mesh is 3.2 counts (approximately 1.5%). Given the large increase in computational cost when performing optimization with the L0 mesh, we decided that the L1 mesh is a good compromise between computational cost and fidelity [18]. This decision is justified by observing the drag reduction from the single point optimization on L0 and L1 meshes is nearly identical. This indicates that the drag improvement predicted by the L1 mesh is entirely realized on the L0 mesh. The grid convergence curves for the two configurations are shown in Figure 4. For this paper, all drag values are given in terms of drag counts, defined as $C_{D_{\text{Counts}}} = 10000 \times C_D$.

Mesh level	Mesh size	Initial C_D	Optimized C_D	$\Delta\, C_D$	C_L	Optimized C_M
$h = 0$	∞	196.95	182.01	-14.94		
L0	$28,835,840$	197.64	182.72	-14.91	0.5000	-0.1689
L1	$3,604,480$	199.71	184.83	-14.88	0.5000	-0.1700
L2	$450,560$	209.40	197.00	-12.40	0.5000	-0.172

Table 1. The drag differences between the initial and optimized meshes are nearly constant for each grid level.

C. Optimization Cases

For the ADODG CRM wing geometry, a total of six optimization cases are defined. The first three are recommended, while the remaining three are considered optional. Case 4.1 is the baseline single point optimization. Results for this case have been reported previously by the authors, and the resulting geometries and meshes are publicly available [18]. This single point case and the new multipoint cases are summarized in Table 2. Cases 4.2 through 4.5 are a series of
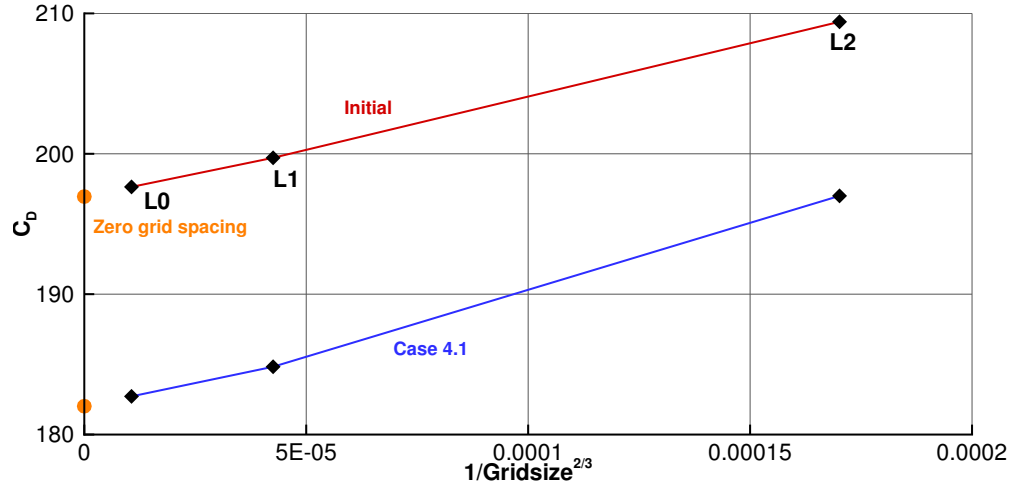
5

Figure 4. The grid convergence study shows that the difference between the 3.6M and zero-mesh spacing value is 3.2 drag counts for the initial design.

multipoint optimizations, each consisting of three different operating conditions. Various combinations of Mach number, C_L and Reynolds number are considered. Case 4.6 is a 9-point optimization combining the operating conditions of cases 4.2 and 4.5, with the addition of the "corners" of the resulting 3×3 pattern in C_L-Mach space. A complete description of each of the cases is given in Table 2.

The design point weights ($\mathcal{T}_i$) for the multipoint cases are derived from a 1-D quadrature rule for the three point cases, and from a 2-D quadrature rule for case 4.6. These weights correspond to performing the numerical integration of C_L over the Mach-C_L space with a uniform continuous weighting function.

The general form of each optimization problem statement can be written as follows, where N is the number of flight conditions considered:

	Function/variable	Description	Quantity
minimize	$\sum\limits_{i=1}^{N} \mathcal{T}_i D_i$	Weighted average drag	
with respect to	x_{shape}	z perturbation in FFD control points	768
	α_i	Angle of attack	N
		Total design variables	**768 + N**
subject to	$C_{L_i} - C_{L_i}^* = 0$	Lift constraints	N
	$C_M \geq -0.17$	Moment constraint at nominal condition	1
	$V \geq V_{\text{init}}$	Volume Constraint	1
	$t_j \geq 0.25 t_{j_{\text{init}}}$	Thickness constraints	750
		Total constraints	**752 + N**

The design variables correspond to those stipulated by the ADODG case description. The shape design variables in our case are the z-coordinate displacements of the FFD volume control points, i.e., these points are allowed to move only in the vertical direction. In addition, each operating condition has an independent angle of attack variable. Equality constraints for the lift coefficient are enforced at each operating condition. A single pitching moment inequality constraint is enforced only at the nominal flight condition (M=0.85, C_L=0.5) for each optimization.

Finally, two types of geometric constraints are imposed: the internal volume of the wing must be greater than or equal to the initial volume, and the thickness of the wing must be greater than or equal to 25% of the initial thickness at any point. In our implementation, the wing internal volume is approximated by discretely adding the volume from a

6

grid of 24×29 hex volumes distributed from the 1% to 99% chord locations whose nodes are projected onto the wing upper and lower surfaces. The thickness constraints are computed in a similar manner: A grid of 25×30 nodes from the 1% to 99% local chord locations are projected vertically onto the upper and lower surfaces. The length of each line segment is then constrained to be greater that 25% of the initial length.

IV.   Results

A.   Multilevel Optimization

In an effort to reduce the overall computational cost of performing the multipoint optimizations, we employ the multilevel optimization approach described previously by the authors [18]. Using this approach, we first perform optimization using a coarse mesh and then use the optimized coarse result as a starting point for the optimization based on a finer grid. This is analogous to the grid sequencing start-up technique often employed in CFD solvers. Due to the much lower cost of performing optimization on the coarse grids, we can afford to do more optimization iterations on the coarse grid. For this approach to be effective, it is essential that the coarse grid be sufficiently resolved to capture the main characteristics of the flow. For the shape design optimizations presented in this paper, this means capturing the shock strength and location, as well as quantifying the drag reduction that is possible by increasing the root thickness and decreasing the tip thickness.
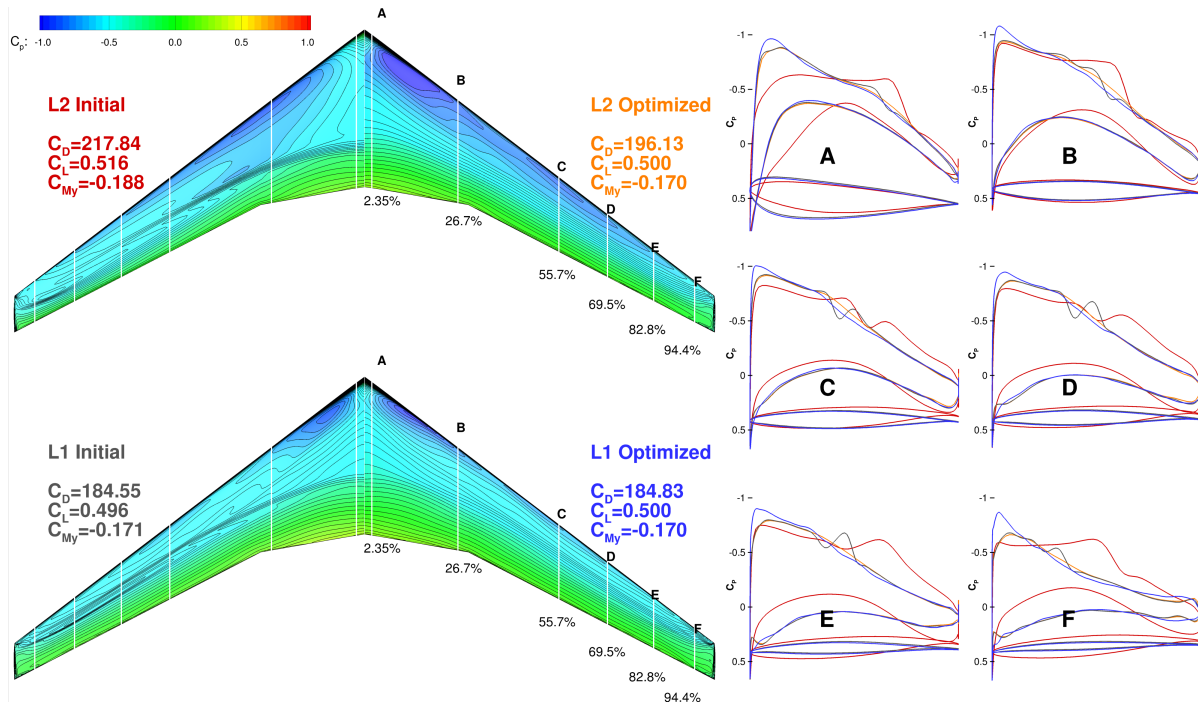

Figure 5. The coarse grid optimum is a good starting point for the fine grid optimization.

A comparison of the initial and optimized designs for this procedure for Case 4.1 is shown in Figure 5. As we can see, the coarse optimization (using the L2 grid) successfully eliminates the shock on the upper wing surface resulting in parallel isobars. Even without further optimization, almost all of the drag improvement predicted by the coarse grid is realized on the fine grid. Comparing the orange and black lines on the C_p distributions we see that the only significant difference is the appearance of a weak shock on the refined grid. The fine optimization further improves the design, eliminating once again this shock and lowering the drag even further. This behavior is consistent with our previous results, which used three grid levels [18]. We employ this multilevel approach for the all the optimization cases in this paper.
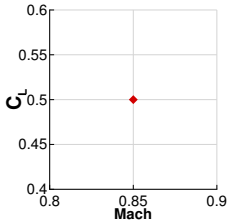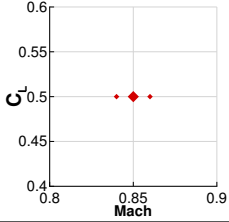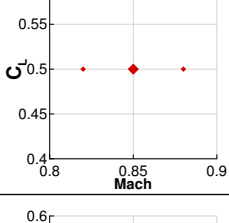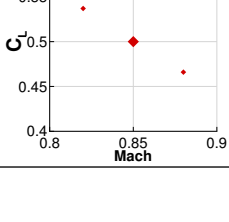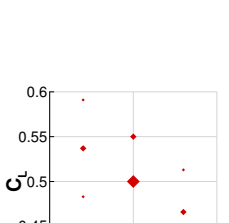
7

B.   Optimization Results

In this section we present the main results from the six CRM wing optimization cases summarized in Table 2. Figure 6 shows the evolution of the SNOPT merit function and optimality. The merit function is used in the augmented Lagrangian formulation and the optimality is a measure of how well the Karush–Kuhn–Tucker (KKT) conditions are satisfied.

The lift, moment, thickness and volume constraints are all satisfied to a tolerance of 1×10^{-5} at the end of each optimization. An average of about 200 iterations were performed for the coarse grid optimizations. This results in two to three orders of magnitude reduction in the optimality. For the L1 optimizations, a fixed iteration limit of 50 imposed, resulting in another one to two orders of magnitude reduction of the optimality tolerance. For most optimizations, the final optimality tolerance of the L1 optimization is the same order of magnitude as the L2 optimality, but on average slightly higher. It is possible that there is still a small amount of improvement that could be made on the fine grid optimizations, but we feel they are sufficiently converged for the purposes of comparison between the optimized designs.

Figures 7 through 12 show a summary of the key features of each optimization. The initial configuration results are shown in red, while the optimized results are shown in blue. The planform view of the wing shows the C_p contours of the initial geometry (left) and the optimized geometry (right) at the nominal operating condition, along with the corresponding drag coefficients. Just below the planform view the front view also shows the C_p contours and adds a visualization of the shock surface [32], as well as the physical thickness variation in the wing. Below this, we plot the spanwise lift, twist, and thickness-to-chord ratio distributions. A reference elliptic lift distribution is shown in gray. The right side of the figure displays the cross-sectional shape and C_p distribution at the six spanwise locations stipulated in the ADODG case description. The leftmost three plots on the bottom of the figure show the polar resulting from an alpha sweep at the nominal Mach number of 0.85. The alpha sweep spans 1.8° to 3.8° in 0.1° increments. Lift, drag and moment curves corresponding to this alpha sweep are displayed. Finally, the bottom right plot shows the drag divergence behavior for three lift coefficients: $C_L = 0.475, 0.50, 0.55$. These curves are extracted using the same data used to generate the ML/cD contours in Figure 14.

Table 2. Operating conditions for each optimization.

| Case	Point	Weights ($\mathcal{T}_i$)	Mach	C_L	Re	C_L-Mach plot
4.1	1	1.0	0.85	0.500	5.00×10^6	
4.2	1	$\frac{1}{4}$	0.85	0.450	5.00×10^6	
	2	$\frac{1}{2}$	0.85	0.500	5.00×10^6	
	3	$\frac{1}{4}$	0.85	0.550	5.00×10^6	
4.3	1	$\frac{1}{4}$	0.84	0.500	5.00×10^6	
	2	$\frac{1}{2}$	0.85	0.500	5.00×10^6	
	3	$\frac{1}{4}$	0.86	0.500	5.00×10^6	
4.4	1	$\frac{1}{4}$	0.82	0.500	5.18×10^6	
	2	$\frac{1}{2}$	0.85	0.500	5.00×10^6	
	3	$\frac{1}{4}$	0.88	0.500	4.83×10^6	
4.5	1	$\frac{1}{4}$	0.82	0.537	4.82×10^6	
	2	$\frac{1}{2}$	0.85	0.500	5.00×10^6	
	3	$\frac{1}{4}$	0.88	0.466	5.18×10^6	
4.6	1	$\frac{1}{16}$	0.82	0.483	4.82×10^6	
	2	$\frac{1}{8}$	0.82	0.537	4.82×10^6	
	3	$\frac{1}{16}$	0.82	0.591	4.82×10^6	
	4	$\frac{1}{8}$	0.85	0.450	5.00×10^6	
	5	$\frac{1}{4}$	0.85	0.500	5.00×10^6	
	6	$\frac{1}{8}$	0.85	0.550	5.00×10^6	
	7	$\frac{1}{16}$	0.88	0.442	5.18×10^6	
	8	$\frac{1}{8}$	0.88	0.466	5.18×10^6	
	9	$\frac{1}{16}$	0.88	0.513	5.18×10^6	

9
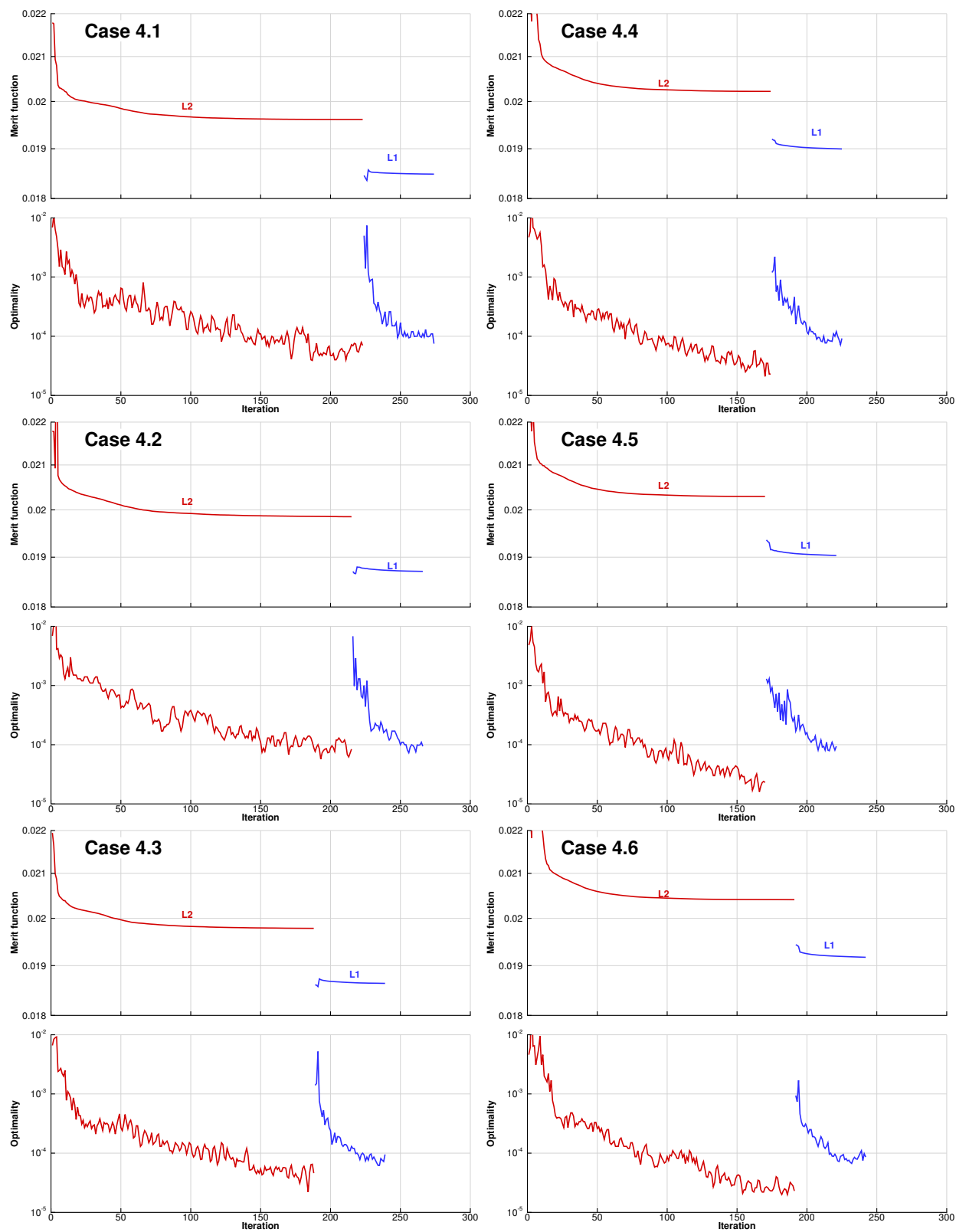
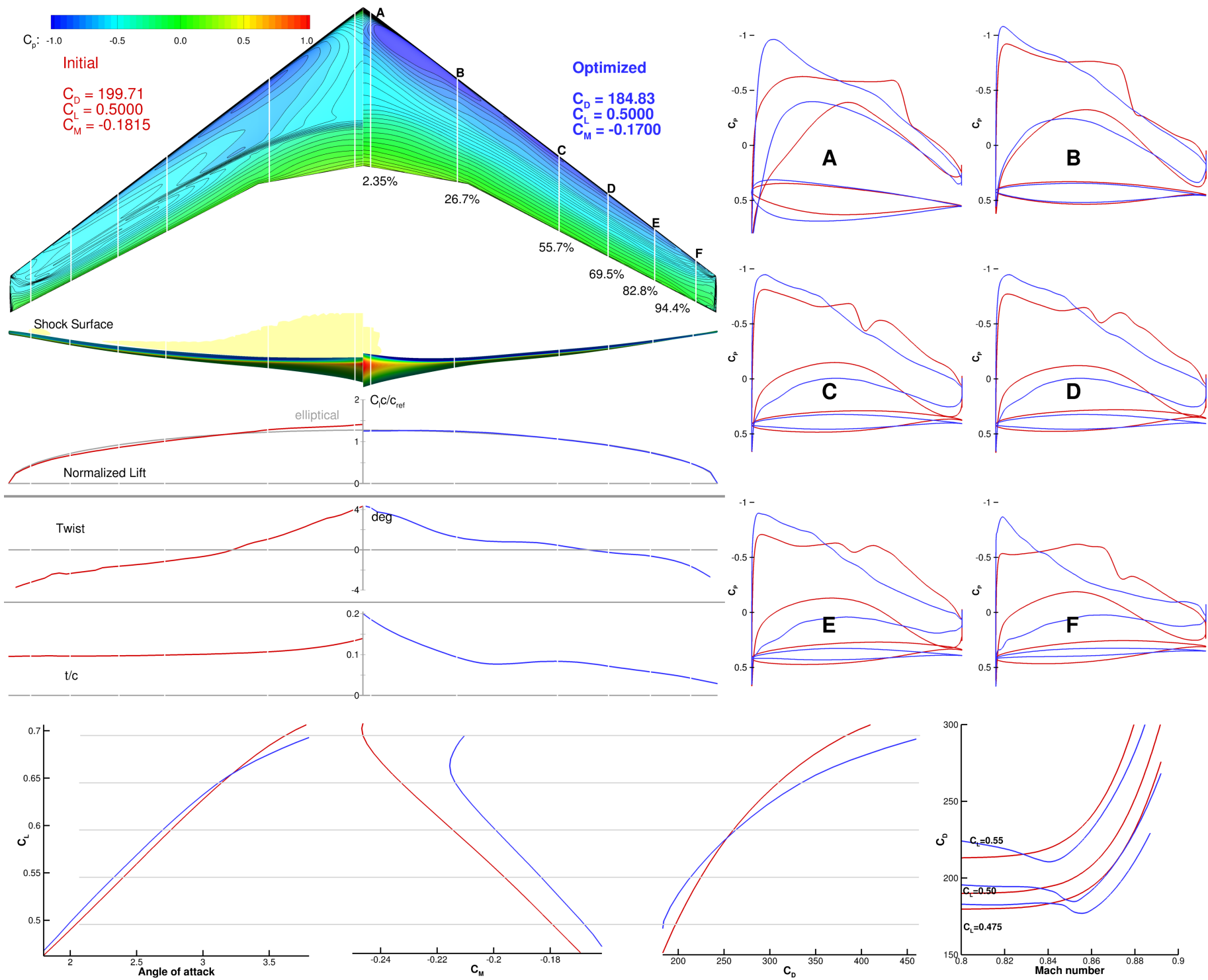**Figure 6. Objective function and optimization evolution for each optimization case.**

Figure 7. Case 4.1 result.

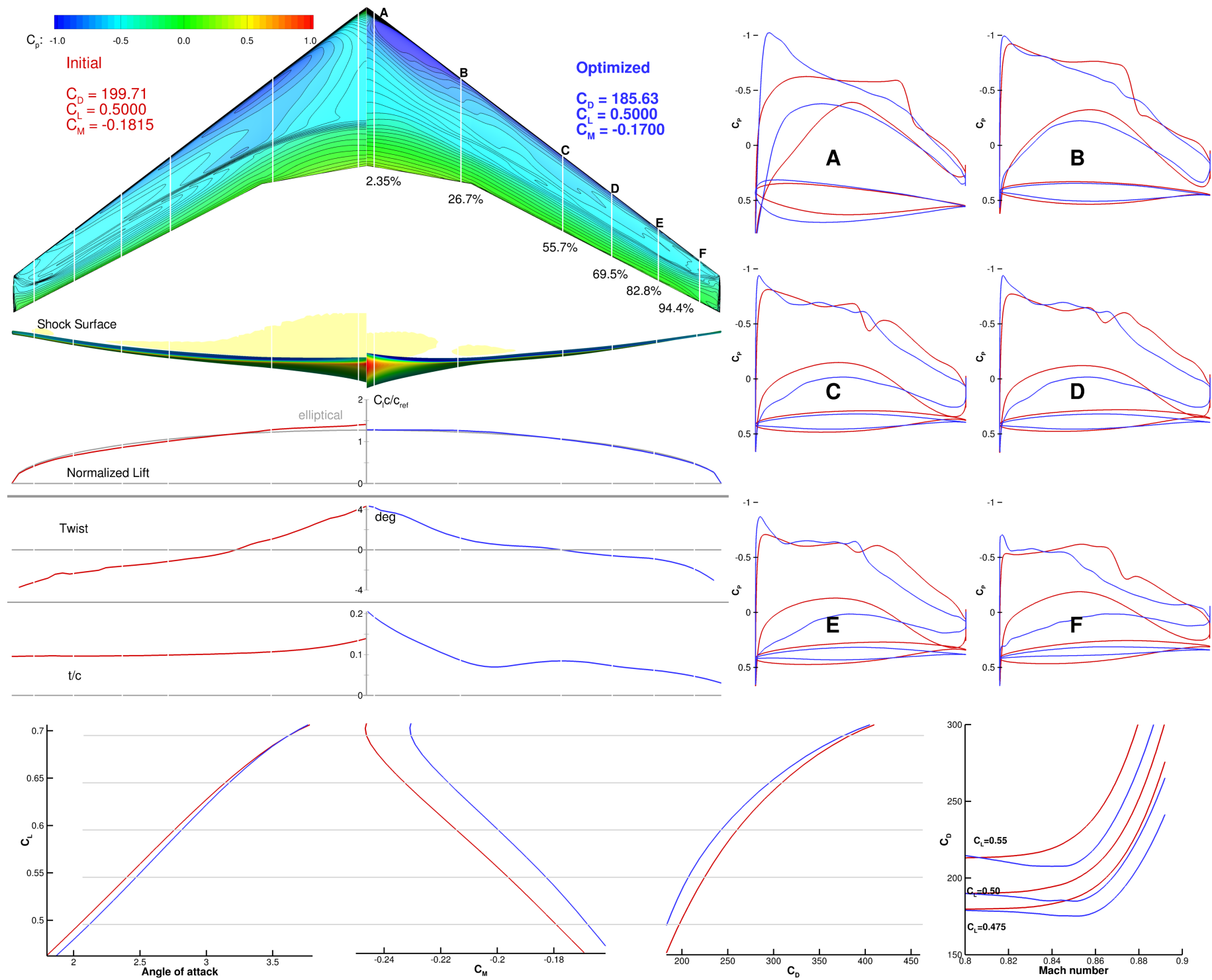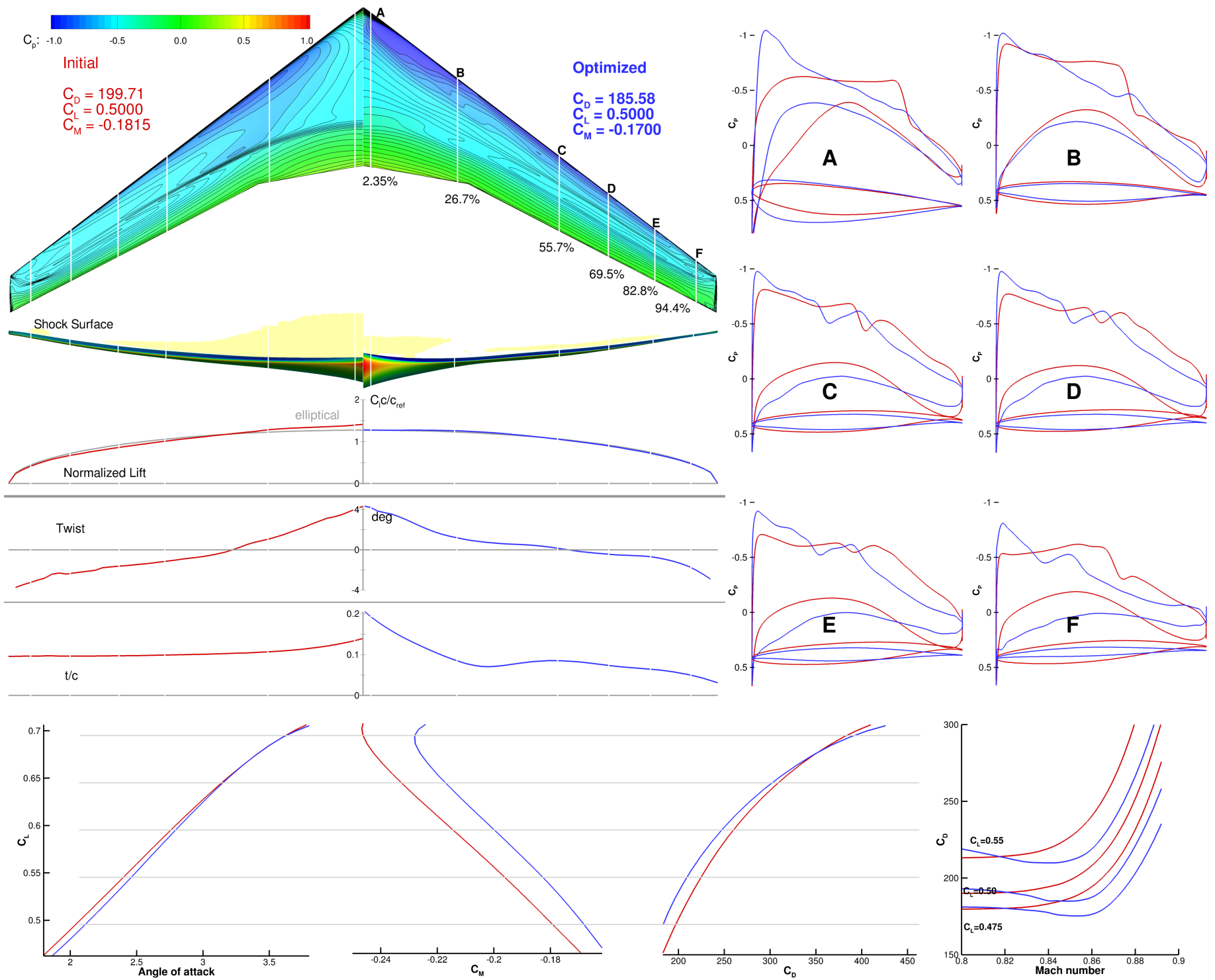**Figure 8.   Case 4.2 result.**

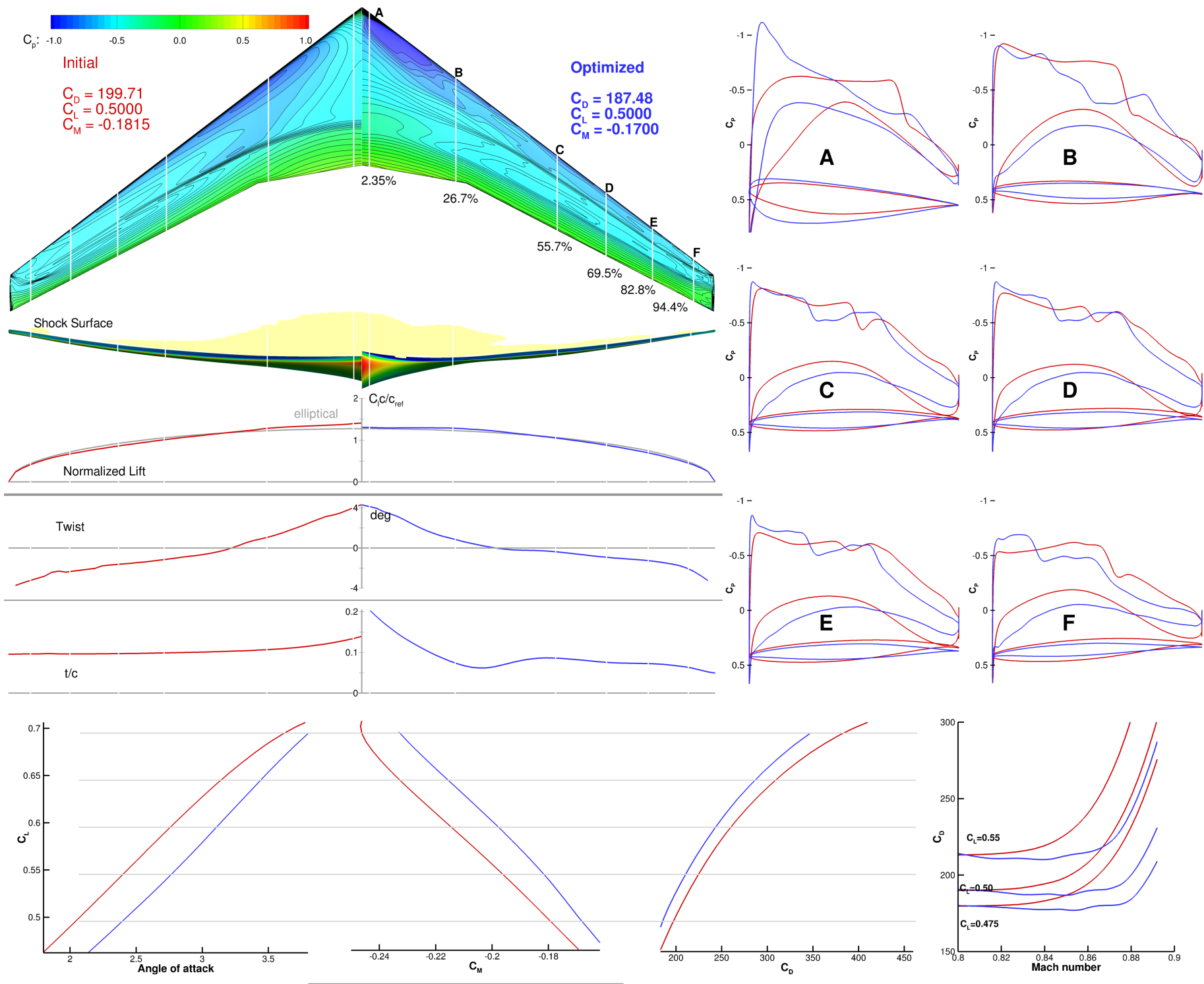**Figure 9. Case 4.3 result.**

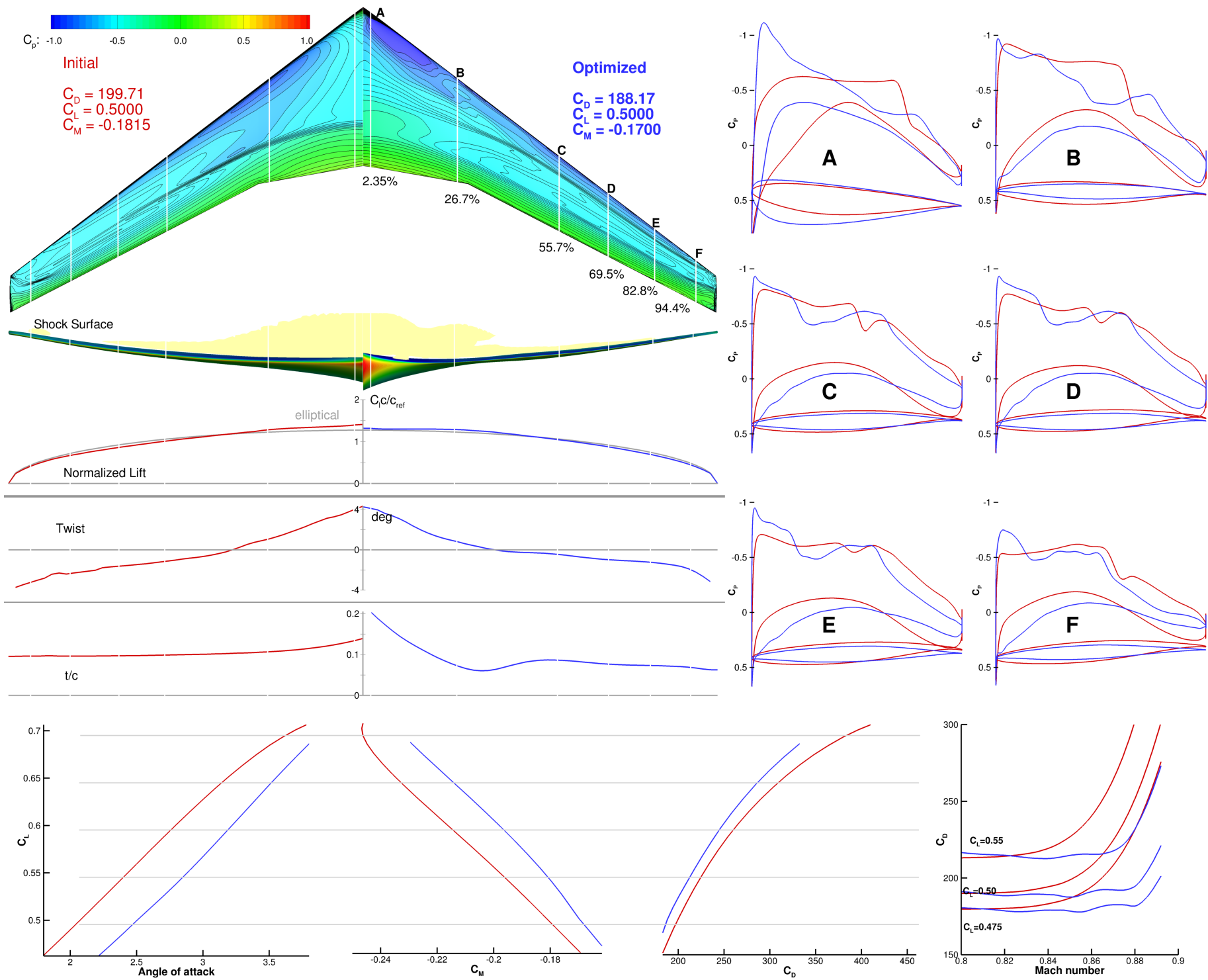**Figure 10. Case 4.4 result.**
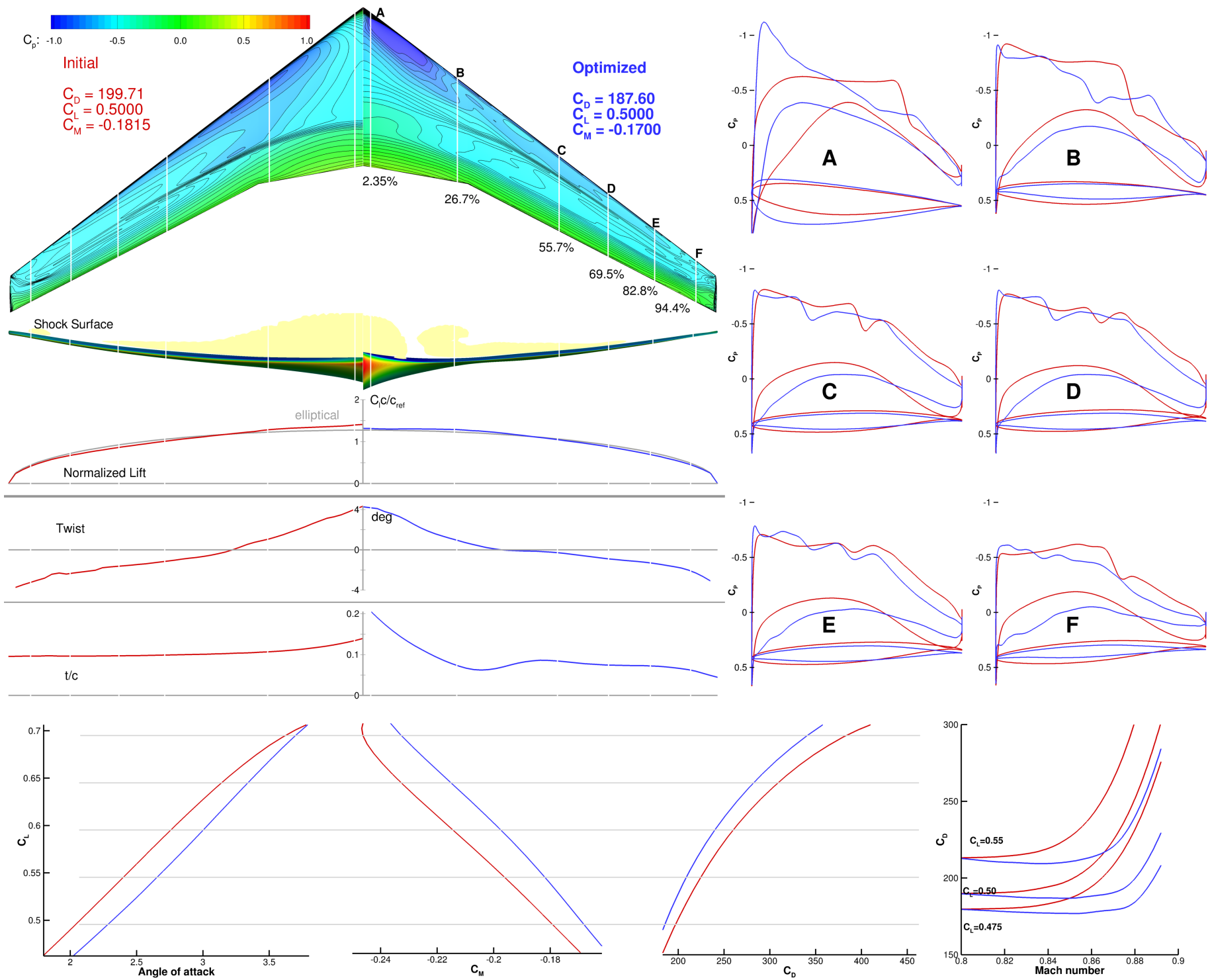
Figure 11. Case 4.5 result.

Figure 12. Case 4.6 result.

There are a few overall trends that are common to all six optimized results. Firstly, all designs result in a significant increase in thickness to chord ratio near the root and a large reduction near the tip. We have previously noticed his behavior for Case 4.1 [18], and the same design trade-off has been made for the multipoint cases as well. Overall, there is no significant change in twist between the initial design and any of the optimized designs. As expected, the lift distribution in Case 4.1, is indistinguishable from an elliptic distribution, which yields the lowest induced drag. The optimizations with closely spaced Mach numbers—Cases 4.2 and 4.3—also have lift distributions that are also close to elliptical. However, the remaining widely spaced optimizations have a slightly less elliptical distribution, but is still closer to elliptical than the initial design.

The shock surface visualization highlights some of the trade-offs the optimization is making. Cases 4.1, 4.2, and 4.3, exhibit weak shocks at the design condition. For the remaining cases, stronger shocks are present at the nominal design condition. Shocks can be seen on all cases except Case 4.1, which is an expected result of a single point optimization. The effect of the aforementioned thickness to chord ratio reduction can be clearly seen in the airfoils, especially in airfoils E and F. The optimization thinned out the airfoils at the tip, especially at the leading edge. This effect is slightly less pronounced in the multipoint designs. This characteristic is highly undesirable from a practical design perspective due to poor low speed $C_{L_{\max}}$ performance.

The previous discussion focused on the large-scale changes to the design. In addition to these common changes, the optimizer has made changes on a much smaller scale to improve local flow characteristics. One particular issue with the initial CRM geometry is that there is a small amount of trailing edge flow separation on the outboard span of the wing at the nominal flight condition. This was done by design to provide an additional challenge for the Drag Prediction Workshop [33]. Through very small shape modifications near the trailing edge, the optimization is able to completely eliminate this flow separation from the nominal operating condition of all six optimizations. This change is shown in Figure 13 for Case 4.1. This demonstrates that our RANS model is able to account for the complex turbulent boundary layer interactions near the trailing edge, and that the numerical optimization can account for local issues and fix them in the pursuit of the minimization of total drag.
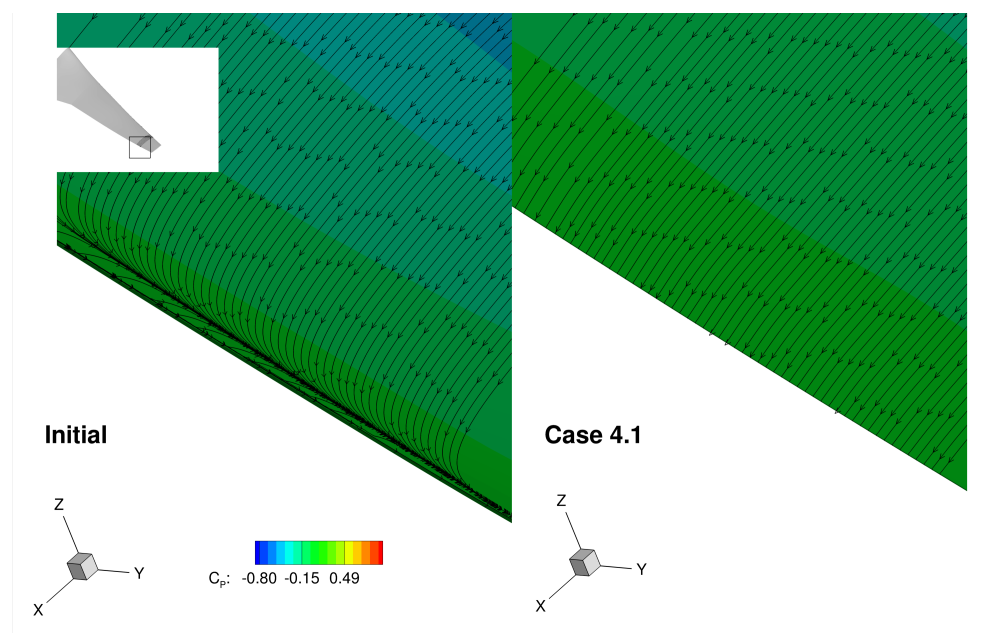

Figure 13. The optimization has corrected a small amount of trailing edge flow separation.

The drag divergence curves for each of the optimized designs yield interesting trends. The single point optimized design has a significant drop around the nominal operating condition. Without any regard to other nearby operating conditions, the drag performance is hindered for off-design conditions. This undesirable characteristic is the motiva-

17

tion for performing multipoint optimization. All of the multipoint optimizations show considerably better off-design performance.

Even with multipoint optimization it is possible see the effects of a particular operating conditions. Case 4.5, and to a lesser extent Case 4.4, shows this clearly. There are three distinct dips in the $C_L = 0.5$ drag curve for Case 4.5 at Mach 0.82, 0.85 and 0.88, which coincide with the selected design Mach numbers. The drag divergence curves for the closely spaced design points (Cases 4.2 and 4.3) do not show this effect as dramatically. However, the drag divergence curves are not lowered over as wide of a range. Finally, Case 4.6 shows a fairly uniform reduction in drag over the three lift coefficients and over the full range of Mach numbers.

While drag divergence curves can yield useful insight into a particular optimized design, it is instructive to examine contours of ML/cD. This is a two-dimensional extension of drag divergence curves, but with an important distinction. In the context of commercial transonic wing design, it is not the actual maximum value of L/D that is important, but rather the range factor, in the Breguet range equation:

$$R = \frac{L}{D}\frac{V}{c}\ln\left(\frac{W_1}{W_2}\right) \tag{1}$$

where L/D is the lift to drag ratio, V is the velocity, c is the thrust specific fuel consumption, and W_1 and W_2 are the initial and final cruise weights, respectively. The range factor is $\frac{L}{D}\frac{V}{c}$. We make the assumption that the speed of sound is constant, which is generally true in the tropopause ($>36\,000$ ft) but is only approximate for lower altitudes. With this assumption, the velocity may be replaced by the Mach number. For the thrust specific fuel consumption, we use a 0-dimensional engine model to estimate the thrust and thrust specific fuel consumption for a high-bypass ratio turbofan, similar to a GE-90. With a fixed ratio fixed ratio $\frac{W_1}{W_2}$, ML/cD may be used a surrogate for the aircraft range.

We evaluate a two dimensional grid of samples in $M - CL_L$ space. Once the drag value is known, the required engine throttle setting to satisfy $T - D = 0$ may be determined and the corresponding thrust specific fuel consumption. To be strictly correct, the additional drag associated with the fuselage, horizontal stabilizer, vertical stabilizer and pylons should be included. In addition, the wing-alone simulation is computed a wind tunnel test Reynolds number of 5 million, not the flight Reynolds number of approximately 40 million. Therefore, for simplicity, these factors are ignored, and the just the CFD computed lift and drag values are used. A comparison of these contours for the initial design and 5 of the optimized designs is given in Figure 14.

Two particular contour values are highlighted. The red contour corresponds to the 99% of the maximum value on the initial design. The motivation to plotting these 99% contours is that airliners typically fly between the Mach number yielding maximum range (approximated by the maximum ML/cD value in the figures) and a higher Mach number that yields a 1% fuel burn drag penalty but a decrease in flight time. In addition, the area enclosed by the 99% contour is a measure of robustness for a given design: Any Mach-C_L combination within the contour incurs no more than a 1% fuel burn penalty. The blue contour is the 99% contour of the optimization's own maximum value.

The performance differences resulting from the different optimizations are now evident. The sharp drag dip for the Case 4.1 is manifested as a small and narrow 99% contour around the nominal operating condition. For this case, the area enclosed by the 37.79 contour is approximately the same as the initial, although it has been shifted to an overall higher Mach number. As expected, the absolute maximum ML/cD value is obtained by the single-point optimized design (Case 4.1). The next highest values are from the closely-spaced design point optimizations (Cases 4.2 and 4.3). For a very small reduction in the maximum ML/cD, a significantly enlarged 99% contour is obtained.

We can also see how the choice of design points influences the shape of the resulting contours. The three C_L values at fixed Mach number in Case 4.2 result in a narrower and taller 99% contour when compared to Case 4.3, which has a wider and shorter contour that closely matches the selected operating conditions. In the interest of conciseness, we only plot Case 4.5, but we observed that Case 4.4 exhibits similar characteristics. In this case, a multimodal operating envelope is created, as the 99% contour exhibits two distinct regions. One region, containing the overall maximum, is near the nominal operating condition. The second one is a small high-performance region near the high-Mach number design point. Case 4.5 has the lowest maximum of the optimized designs, presumably due to difficulties in reducing the drag at the high Mach number operating condition.

The 9-point optimization (Case 4.6), despite containing the same three operating conditions as Case 4.5, shows much more robust behavior. While this design does have the second lowest maximum value, it is the most robust of the optimized designs when considering the area enclosed by the 99% contour, and is fairly close in size to the 99% contour of the initial design.
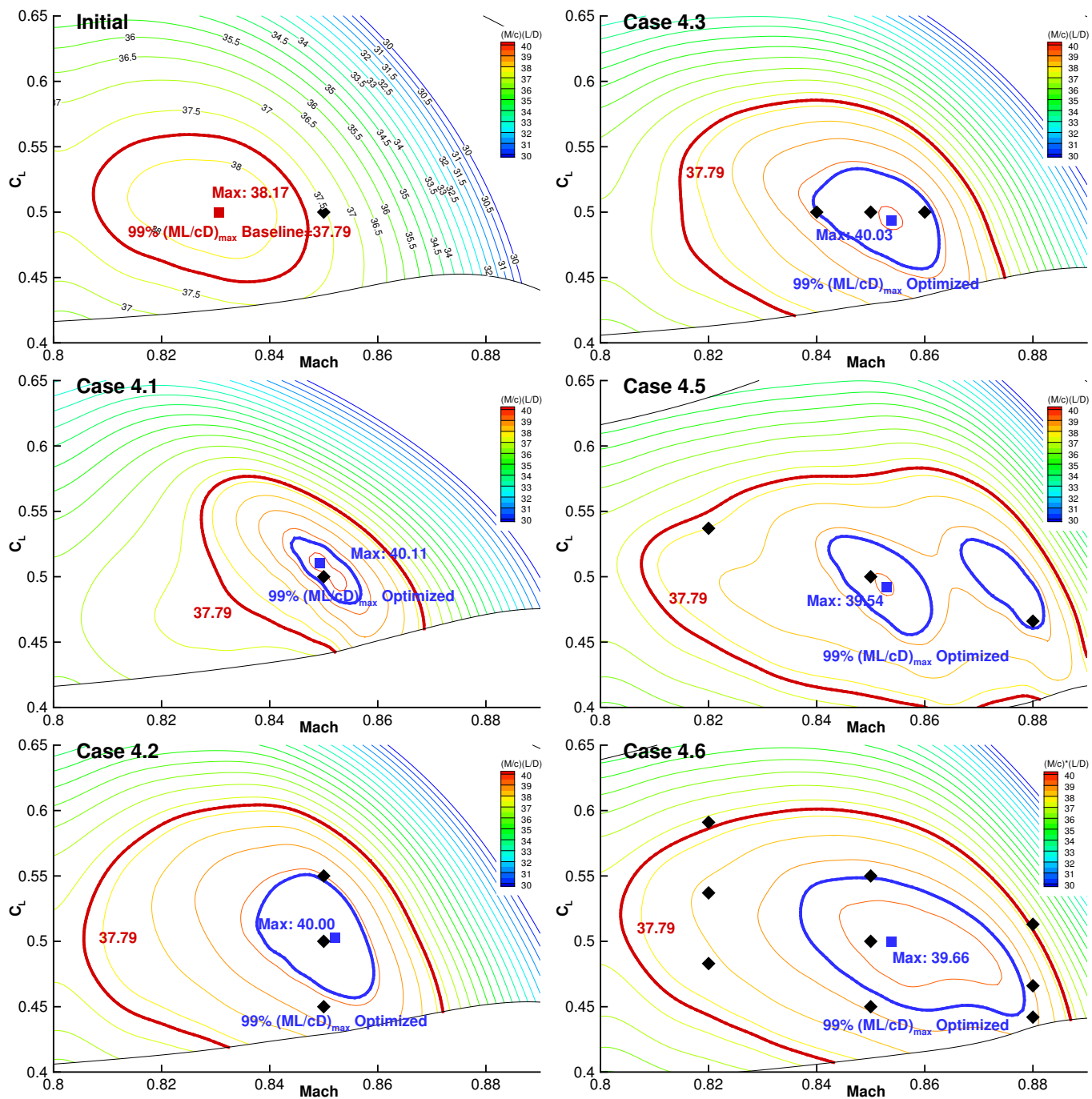
Figure 14. ML/cD **contours for the initial and optimized geometries. Contour lines are spaced at 0.5 intervals.**

Figure 15 demonstrates how all optimized designs are markedly less robust than the initial design as indicated by the size of the 99% contour. However, the 9-point design achieved a robustness that is almost as good as the initial design. Furthermore, it achieves this performance at a Mach number much closer to the desired nominal.

While Case 4.6 appears to be robust, the comparison in Figure 15 is not entirely fair: The maximum value for Case
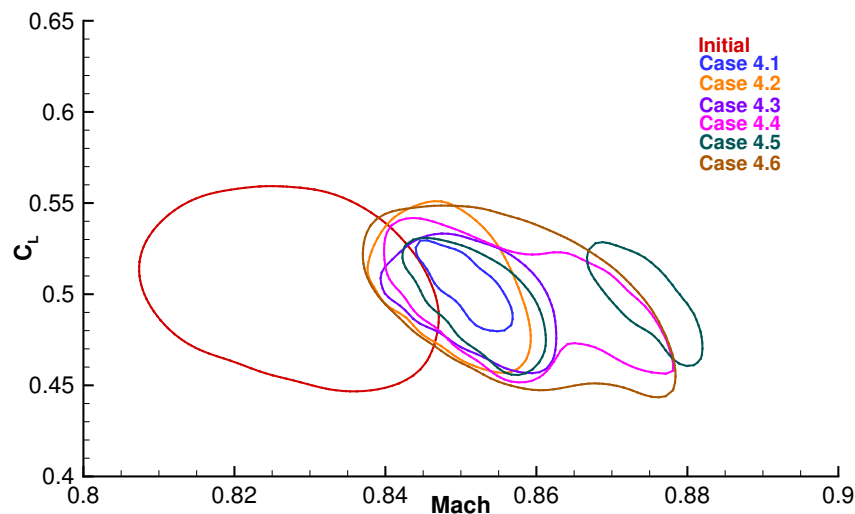
19

Figure 15. $0.99(ML/cD)_{\mathbf{max}}$ **contours for the initial and optimized geometries.**

4.6 is only 99.08% of the maximum value Case 4.2. For a more appropriate comparison, we compare the 99% contour value from case 4.6 (39.26) for all optimized designs. This is given in Figure 16.
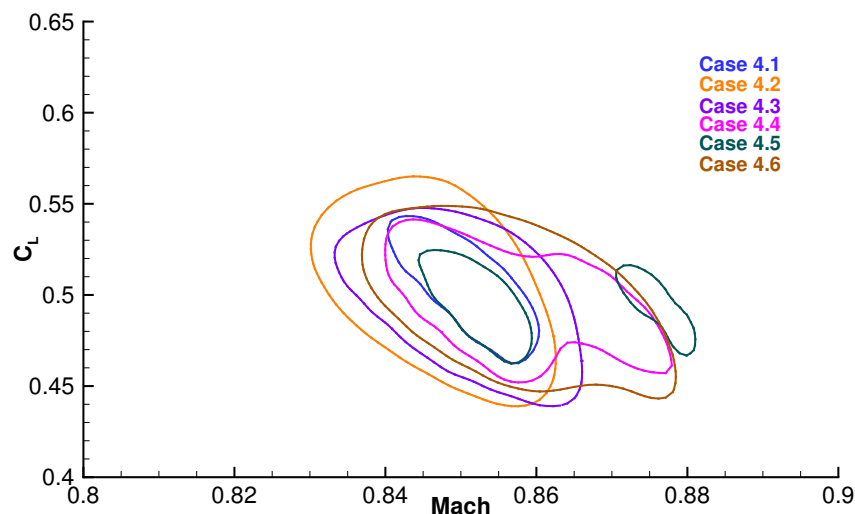

Figure 16. $(ML/cD)_{\mathbf{max}} = 39.26$ **contours for the optimized geometries.**

For this fixed-performance comparison, the closely spaced optimizations Cases 4.2 and 4.3 now compare much more favorably with the 9-point optimization. Case 4.2, which includes three C_L values at the same Mach number appears to be more effective than three different Mach numbers at the same C_L. Unsurprisingly, only the cases that included design points at the Mach=0.88 operating condition (Cases 4.4 through 4.6) show consistently good performance up to and including Mach=0.88. For optimizations with widely spaced Mach numbers, it appears that the nine design points are required to produce a robust design. However, if a smaller operational envelope is acceptable as characterized by Case 4.2 and Case 4.3 optimizations, three optimization design points may be sufficient.

For this particular set of optimization problem we can draw a few general conclusions with respect to the number and distribution of operating conditions. It is clear the single point design results in a particularly poorly robust design, even if the peak performance is higher. All three point optimizations remedied this situation with the widely spaced optimized (Case 4.5 and 5.5) yielding larger 99% contours, although the multimodal characteristic is probably undesirable. Since the closely spaced optimizations (Case 4.2 and 4.3) have only a 0.28% penalty in the peak value compared to Case 4.2, they are more desirable than Cases 4.4 and 4.5. Case 4.6 is the most desirable from a robustness perspective, although this comes with approximately three times higher computational cost.

We must caution however, that all these optimization cases are of only academic interest and are not representative of real aerodynamic shape optimization for an actual transonic aircraft configuration for several reasons. Firstly, the lack of the fuselage results in an incorrect lift distribution. In fact, the initial CRM when combined with the fuselage has a closer to elliptic lift distribution than the wing alone without the fuselage presence [15, 34]. Secondly, the analysis is performed at a wind-tunnel Reynolds number of 5 M, as opposed to a flight Reynolds number of approximately 40 M. It is not known what effect this would have on the optimal design. Thirdly, the 25% lower bound on the thickness constraints is impractical. In reality, an internal structure would be required to support the wing loads and the optimized thickness distributions would result in considerable structural difficulties both in static and dynamic phenomena. Finally, an aircraft wing is not rigid and deforms according to the actual flight loads. This bends and twists the wing, resulting in a different spanwise lift distribution, shock structure and induced drag. Previous work by the authors have investigated optimizations that address the shortcomings of these aerodynamic only optimizations by performing aerostructural optimization, but this is out of the scope of the ADODG benchmarks [15, 9, 10, 11].

C. Computational Cost

Multipoint three-dimensional RANS-based aerodynamic shape optimizations are costly from an computational perspective. We make every effort to reduce the total computational cost of performing the optimizations herein. Table 3 lists the total CPU cost, in processors hours, required to generate all results presented in this paper. All computations were performed on the Gordon Compute Cluster at the San Diego Supercomputer Center [35]. Each computational node consists of two Intel E5-2670 CPUs running at 2.6 GHz with 64 GB of DDR3-1333 MHz RAM. The nodes are connected with 4X QDR InfiniBand. All analysis using the L2 grid utilized 16 cores (1 node), while all analysis using the L1 grid utilized 64 cores (4 nodes).

Table 3. Computational cost breakdown in CPU-hours.

Case	L2 optimization	L1 optimization	α-Mach sweeps	Contour	Total
Initial	–	–	820	3 234	4 054
4.1	344	1 088	580	2 629	4 641
4.2	935	3 023	638	3 308	7 904
4.3	825	3 266	624	2 700	7 414
4.4	820	3 441	597	3 247	8 105
4.5	809	3 508	676	3 236	8 229
4.6	2 631	10 053	1 850	2 777	17 311
Total	6 363	24 380	5 768	21 131	**57 659**

Just over half of the total computational cost is allocated to the optimizations, and the remainder was used for post processing. The ML/cDD contour plots are particularly costly, as each requires 552 individual CFD evaluations. The contour plots are evaluated by performing 24 α sweeps at different Mach numbers, each with 23 α values.

V. Conclusions

In this paper, we presented a series of six optimizations of increasing complexity from the CRM wing shape optimization benchmark defined by the Aerodynamic Design Optimization Discussion Group (ADODG). The weighted average drag was minimized with respect to 768 shape design variables, subject to lift, pitching moment, volume, and

21

thickness constraints. A two-level optimization approach was used: Coarse grid optimizations were carried out on a 450 k cell mesh, followed by a second and final optimization using a 3.6 M cell mesh.

At the nominal design operating condition of $M = 0.85$, C_L=0.5, the single point optimization reduced the drag coefficient by 7.5% from 199.7 counts to 184.83. All remaining multipoint optimizations traded drag improvement at the nominal condition for increased performance over a wider range of operating conditions.

An effective way of comparing optimized designs is to plot contours of constant ML/cD performance in the M-C_L plane. This is a good measure to use when comparing wings designed for transonic flow conditions, as it approximates the range factor of the Breguet range equation. The 99% contour of the maximum ML/cD value was used to give an indication of the robustness of each optimized design. The single point design had the highest range factor, but was the least robust of the optimized designs. The closely spaced 3-point optimizations (Cases 4.2 and 4.3) were a good trade-off between increasing the robustness of the design while lowering the maximal value by less than 0.3%. One of the two widely spaced design point optimizations (Case 4.5) showed two peaks in ML/cD, indicating multimodal performance. In essence, this optimization combined 3-point designs in the same geometric shape. Finally, the most robust performance was obtained by the 9-point optimization (Case 4.6). The increased number of operating conditions at different C_L's mitigated the effects of the widely spaced operating conditions of Cases 4.4 and 4.5. The robustness of this design was determined by the area enclosed inside of the 99% contour, which compared favorably with the initial design.

VI.   Acknowledgments

References

[1] Pironneau, O., "On Optimum Profiles in Stokes Flow," *Journal of Fluid Mechanics*, Vol. 59, No. 01, 1973, pp. 117–128. doi:10.1017/S002211207300145X.

[2] Jameson, A., "Aerodynamic Design via Control Theory," Vol. 3, No. 3, 1988, pp. 233–260. doi:10.1007/BF01061285.

[3] Nielsen, E. J. and Anderson, W. K., "Aerodynamic Design Optimization on Unstructured Meshes Using the Navier–Stokes Equations," *AIAA Journal*, Vol. 37, No. 11, 1999, pp. 1411–1419.

[4] Anderson, W. K. and Venkatakrishnan, V., "Aerodynamic Design Optimization on Unstructured Grids with a Continuous Adjoint Formulation," *Computers and Fluids*, Vol. 28, No. 4, 1999, pp. 443–480.

[5] Peter, J. E. V. and Dwight, R. P., "Numerical Sensitivity Analysis for Aerodynamic Optimization: A Survey of Approaches," *Computers and Fluids*, Vol. 39, 2010, pp. 373–391. doi:10.1016/j.compfluid.2009.09.013.

[6] Lyu, Z., Kenway, G. K., and Martins, J. R. R. A., "Aerodynamic Shape Optimization Studies on the Common Research Model Wing Benchmark," *AIAA Journal*, 2014. doi:10.2514/1.J053318, (In press).

[7] Mader, C. A., Martins, J. R. R. A., Alonso, J. J., and van der Weide, E., "ADjoint: An Approach for the Rapid Development of Discrete Adjoint Solvers," *AIAA Journal*, Vol. 46, No. 4, April 2008, pp. 863–873. doi:10.2514/1.29123.

[8] Lyu, Z., Kenway, G. K., Paige, C., and Martins, J. R. R. A., "Automatic Differentiation Adjoint of the Reynolds-Averaged Navier–Stokes Equations with a Turbulence Model," *21st AIAA Computational Fluid Dynamics Conference*, San Diego, CA, Jul 2013. doi:10.2514/6.2013-2581.

[9] Kenway, G. K. W., Kennedy, G. J., and Martins, J. R. R. A., "Scalable Parallel Approach for High-Fidelity Steady-State Aeroelastic Analysis and Derivative Computations," *AIAA Journal*, Vol. 52, No. 5, May 2014, pp. 935–951. doi:10.2514/1.J052255.

[10] Liem, R., Kenway, G. K. W., and Martins, J. R. R. A., "Multi-mission Aircraft Fuel Burn Minimization via Multi-point Aerostructural Optimization," *AIAA Journal*, 2014, (In press).

[11] Kenway, G. K. W. and Martins, J. R. R. A., "Multipoint High-Fidelity Aerostructural Optimization of a Transport Aircraft Configuration," *Journal of Aircraft*, Vol. 51, No. 1, January 2014, pp. 144–160. doi:10.2514/1.C032150.

[12] Vassberg, J. and Jameson, A., "Influence of Shape Parameterization on Aerodynamic Shape Optimization," Tech. rep., Von Karman Institute, Brussels, Belgium, April 2014.

[13] Telidetzki, K., Osusky, L., and Zingg, D. W., "Application of Jetstream to a Suite of Aerodynamic Shape Optimization Problems," *52nd Aerospace Sciences Meeting*, Feb 2014. doi:10.2514/6.2014-0571.

[14] Carrier, G., Destarac, D., Dumont, A., Meheut, M., Din, I. S. E., Peter, J., Khelil, S. B., Brezillon, J., and Pestana, M., "Gradient-Based Aerodynamic Optimization with the elsA Software," *52nd Aerospace Sciences Meeting*, Feb 2014. doi:10.2514/6.2014-0568.

[15] Kenway, G. K. W. and Martins, J. R. R. A., "Multipoint High-fidelity Aerostructural Optimization of a Transport Aircraft Configuration," *Journal of Aircraft*, Vol. 51, No. 1, 2014, pp. 144–160. doi:10.2514/1.C032150.

[16] Mader, C. A. and Martins, J. R. R. A., "Stability-Constrained Aerodynamic Shape Optimization of Flying Wings," *Journal of Aircraft*, Vol. 50, No. 5, September 2013, pp. 1431–1449. doi:10.2514/1.C031956.

[17] Mader, C. A. and Martins, J. R. R. A., "Computing Stability Derivatives and their Gradients for Aerodynamic Shape Optimization," *AIAA Journal*, Vol. 52, No. 11, November 2014, pp. 2533–2546. doi:10.2514/1.J052922.

[18] Lyu, Z. and Martins, J. R. R. A., "Aerodynamic Design Optimization Studies of a Blended-Wing-Body Aircraft," *Journal of Aircraft*, Vol. 51, No. 5, September 2014, pp. 1604–1617. doi:10.2514/1.C032491.

[19] Kenway, G. K. W., Kennedy, G. J., and Martins, J. R. R. A., "Aerostructural optimization of the Common Research Model configuration," *15th AIAA/ISSMO Multidisciplinary Analysis and Optimization Conference*, Atlanta, GA, June 2014, AIAA 2014-3274.

[20] Osusky, L. M., *A Novel Numerical Tool for Aerodynamic Shape Optimization in Turbulent Flow*, Ph.D. thesis, University of Toronto, 2013.

[21] Martins, J. R. R. A., Alonso, J. J., and Reuther, J. J., "High-Fidelity Aerostructural Design Optimization of a Supersonic Business Jet," *Journal of Aircraft*, Vol. 41, No. 3, 2004, pp. 523–530. doi:10.2514/1.11478.

[22] Kenway, G. K., Kennedy, G. J., and Martins, J. R. R. A., "A CAD-free Approach to High-Fidelity Aerostructural Optimization," *Proceedings of the 13th AIAA/ISSMO Multidisciplinary Analysis Optimization Conference, Fort Worth, TX*, 2010. doi:10.2514/6.2010-9231.

[23] de Boor, C., *A Practical Guide to Splines*, Springer, New York, 2001.

[24] Kenway, G. K., Kennedy, G. J., and Martins, J. R. R. A., "A CAD-free Approach to High-Fidelity Aerostructural Optimization," *Proceedings of the 13th AIAA/ISSMO Multidisciplinary Analysis Optimization Conference, Fort Worth, TX*, 2010. doi:10.2514/6.2010-9231.

[25] van der Weide, E., Kalitzin, G., Schluter, J., and Alonso, J., "Unsteady Turbomachinery Computations Using Massively Parallel Platforms," *44th AIAA Aerospace Sciences Meeting and Exhibit*, 2006. doi:10.2514/6.2006-421.

[26] Jameson, A., Schmidt, W., and Turkel, E., "Numerical Solution of the Euler equations by Finite Volume Methods Using Runge Kutta Time Stepping Schemes," *14th AIAA, Fluid and Plasma Dynamics Conference*, 1981.

[27] Spalart, P. and Allmaras, S., "A One-Equation Turbulence Model for Aerodynamic Flows," *30th Aerospace Sciences Meeting and Exhibit*, 1992. doi:10.2514/6.1992-439.

[28] Lyu, Z., Xu, Z., and Martins, J. R. R. A., "Benchmarking Optimization Algorithms for Wing Aerodynamic Design Optimization," *Proceedings of the 8th International Conference on Computational Fluid Dynamics*, Chengdu, Sichuan, China, July 2014, ICCFD8-2014-0203.

[29] Gill, P. E., Murray, W., and Saunders, M. A., "SNOPT: An SQP Algorithm for Large-Scale Constrained Optimization," *SIAM Journal on Optimization*, Vol. 12, No. 4, 2002, pp. 979–1006. doi:10.1137/S1052623499350013.

[30] Perez, R. E., Jansen, P. W., and Martins, J. R. R. A., "pyOpt: a Python-Based Object-Oriented Framework for Nonlinear Constrained Optimization," *Structural and Multidisciplinary Optimization*, Vol. 45, No. 1, January 2012, pp. 101–118. doi:10.1007/s00158-011-0666-3.

[31] Chan, W. M. and Steger, J. L., "Enhancements of a three-dimensional hyperbolic grid generation scheme," *Applied Mathematics and Computation*, Vol. 51, No. 23, 1992, pp. 181 – 205. doi:http://dx.doi.org/10.1016/0096-3003(92)90073-A.

[32] Haimes, R., "Automated Feature Extraction from Transient CFD Simulations," *Proceeding of the 7th Annual Conference of the CFD Society of Canada, Halifax, NS*, May 1999.

[33] Vassberg, J. C., DeHaan, M. A., Rivers, S. M., and Wahls, R. A., "Development of a Common Research Model for Applied CFD Validation Studies," 2008, AIAA 2008-6919.

[34] Chen, S., Lyu, Z., Kenway, G. K. W., and Martins, J. R. R. A., "Simultaneous Aerodynamic Shape Optimization of the Wing and Horizontal-Tail," *Proceedings of AIAA SciTech 2015*, Kissimmee, FL, January 2015, (abstract submitted).

[35] Towns, J., Cockerill, T., Dahan, M., Foster, I., Gaither, K., Grimshaw, A., Hazlewood, V., Lathrop, S., Lifka, D., Peterson, G., Roskies, R., Scott, J., and Wilkens-Diehr, N., "XSEDE: Accelerating Scientific Discovery," *Computing in Science Engineering*, Vol. 16, No. 5, Sept 2014, pp. 62–74. doi:10.1109/MCSE.2014.80.